

# The Aerosol Limb Imager: acousto-optic imaging of limb scattered sunlight for stratospheric aerosol profiling

B. J. Elash, A. E. Bourassa, P. R. Loewen, N. D. Lloyd, and D. A. Degenstein

Institute of Space and Atmospheric Studies, Saskatchewan, Canada

*Correspondence to:* B. J. Elash (brenden.elash@usask.ca)

**Abstract.** The Aerosol Limb Imager (ALI) is an optical remote sensing instrument designed to image scattered sunlight from the atmospheric limb. These measurements are used to retrieve spatially resolved information of the stratospheric aerosol distribution, including spectral extinction coefficient and particle size. Here we present the design, development and test results of an ALI prototype instrument. The long term goal of this work is the eventual realization of ALI on a satellite platform in low earth orbit, where it can provide high spatial resolution observations, both in the vertical and cross-track. The instrument design uses a large aperture Acousto-Optic Tunable Filter (AOTF) to image the sunlit stratospheric limb in a selectable narrow wavelength band ranging from the visible to the near infrared. The ALI prototype was tested on a stratospheric balloon flight from the Canadian Space Agency (CSA) launch facility in Timmins, Canada, in September 2014. Preliminary analysis of the hyperspectral images ~~indicate~~ indicates that the radiance measurements are of high quality, and we have used these to retrieve vertical profiles of stratospheric aerosol extinction coefficient from 650–1000 nm, along with one moment of the particle size distribution. Those preliminary results are promising and development of a satellite prototype of ALI within the Canadian Space Agency is ongoing.

## 1 Introduction

Stratospheric aerosol plays an important role in the global radiative forcing balance by scattering solar irradiation and causing an overall cooling effect that depends on the particle size distribution and the concentration (Kiehl and Briegleb, 1993; Stocker et al., 2013). These climate effects are an important and recent focus of research due to the potential contribution of stratospheric aerosol to the so-called global warming hiatus (Solomon et al., 2011; Haywood et al., 2014; Fyfe et al., 2013), and efforts to quantify the variability and trends in the global stratospheric aerosol load are underway with various ground based and satellite data sets (Rieger et al., 2015; Ridley et al., 2014).

Since its discovery with stratospheric balloon observations (Junge et al., 1961), stratospheric aerosol has been measured with various techniques, although due to the variability of physical composition and particle size, ~~the observations are essentially always limited to some degree~~ no single measurement technique can fully determine the full range of aerosol properties unambiguously. In-situ balloon observations continue to be used and have provided highly valuable data sets, including most notably the long time series of optical particle counter measurements from Laramie, WY (Deshler et al., 2003, 2006; Kovi-lakam et al., 2015). Aircraft-borne nephelometers (Beuttell and Brewer, 1949; Charlson et al., 1969) acquire detailed in-situ

measurements, providing, for example, plume composition (Murphy et al., 2014), but are spatially limited to the aircraft track. Ground based lidars have been used to do detailed studies of the extent of volcanic aerosol plumes (Chazette et al., 1995; Sawamura et al., 2012) and provide valuable insight into long term local variability and trends in the aerosol layer. For example, lidar observations were used by Hofmann et al. (2009) to first report the observed increase in stratospheric aerosol over approximately the last decade. However, the global distribution, which can only really be obtained with satellite observations, provides invaluable insight into aerosol processes and variability. A good example of this is the use of satellite observations by Vernier et al. (2011b) to determine that the increased stratospheric aerosol load reported by Hofmann et al. (2009) was in fact due to a series of relatively minor, mostly tropical, volcanic eruptions.

Satellite instrumentation capable of remote sensing stratospheric aerosol has been in use since the ~~1970's~~1970s, beginning with limb sounding solar occultation measurements. These have provided a reliable, accurate and essentially continuous long term record of vertically resolved aerosol extinction coefficient measurements, mostly from the series of Stratospheric Aerosol and Gas Experiment (SAGE) instruments (Russell and McCormick, 1989; Thomason and Taha, 2003). These SAGE measurements, which have a vertical resolution of approximately 1 km, have generally compared well with ground based and in-situ measurements, although there are challenges associated with ~~comparing the retrieved extinction profiles to other microphysical parameters~~determining microphysical parameters and comparison between instruments can be significant different. (Russell and McCormick, 1989; Kovilakam et al., 2015). However, solar occultation is generally a robust and stable technique as it directly measures atmospheric optical depth, along with the exo-atmospheric solar spectrum with each scan, allowing for ~~straight forward~~straightforward retrieval of aerosol extinction coefficient (Damadeo et al., 2013). ~~Although the~~The SAGE III mission came to an end in 2006 and the occultation measurements have continued from the currently operational MAESTRO and ACE-20 Imager instruments on SciSat (McElroy et al., 2007; Gilbert et al., 2007) and have had some success producing stratospheric aerosol extinction products (Vanhellemont et al., 2008; Sioris et al., 2010), ~~the era of solar occultation measurements essentially came to an end with SAGE III in 2006. However~~Furthermore, a manifestation of SAGE III is planned for deployment on the International Space Station in 2016 (Cisewski et al., 2014).

More recently, limb scattered sunlight measurements have been used for stratospheric aerosol retrievals. Although this technique has the advantage of being able to sample the atmosphere throughout the sunlit hemisphere, it requires the use of a complex forward model of multiple scattering processes along with at least some a priori knowledge of the aerosol scattering cross section in order to retrieve the extinction coefficient profile. The Optical Spectrograph and InfraRed Imaging System (OSIRIS) instrument (Llewellyn et al., 2004), which was launched in 2001 and is presently still operational, was the first satellite limb scatter instrument to retrieve stratospheric aerosol extinction (Bourassa et al., 2007). The current OSIRIS version 5.07 data product, which provides 750 nm extinction profiles at approximately 2 km vertical resolution, has been shown to agree relatively well, generally within 15%, with SAGE II and SAGE III occultation measurements (Bourassa et al., 2012b; Rieger et al., 2015). The SCanning Imaging Absorption spectroMeter for Atmospheric CHartography (SCIAMACHY) instrument on Envisat (Bovensmann et al., 1999) uses a retrieval technique essentially similar to OSIRIS to retrieve aerosol profiles at 750 nm with approximately 3 km vertical resolution (Taha et al., 2011; Ernst et al., 2012; von Savigny et al., 2015)

from scattered sunlight spectra. SCIAMACHY observations ceased with the demise of Envisat in 2012 and although OSIRIS continues to operate, it is now in the fourteenth year of a mission designed for two years.

The most recently launched limb scatter instrument is the Ozone Mapping Profiler Suite Limb Profiler (OMPS-LP) on the Suomi-NPP satellite. Although similar in spectral range and vertical resolution to OSIRIS, OMPS-LP is an imaging spectrometer that vertically images the limb in a single measurement. Both OSIRIS and SCIAMACHY are grating spectrometers with a narrow field of view, such that limb profiles are obtained by vertically scanning through a range of tangent altitudes. The imaging capability of OMPS provides a decrease in the time required to obtain a limb profile and so increases the along track sampling. Recent work on the feasibility of aerosol retrieval from OMPS-LP measurements show promising results (Rault and Loughman, 2013).

Several recent studies have highlighted the requirement for continued global stratospheric aerosol observations, and especially the need to resolve, both vertically and horizontally, aerosol in the lowermost stratosphere and the upper troposphere. This is the case for tracking the evolution of aerosol from volcanic eruptions, which can have a substantial effect on the aerosol optical depth in the lowermost stratosphere (Ridley et al., 2014; Andersson et al., 2015). Furthering the understanding of the transport of aerosol near and across the tropopause would also benefit from higher spatial and temporal resolution observations. This is evident in the case of volcanic plumes, such as that from Nabro in 2011, the transport and origin of which has been studied extensively and [the conclusions are](#) somewhat controversially (Bourassa et al., 2012c, 2013; Vernier et al., 2013; Fromm et al., 2013, 2014; Fairlie et al., 2014; Clarisse et al., 2014). However, this is also the case for the formation of background-level aerosol, particularly in the region of the Asian and North American monsoons, which have been identified as a source of substantial, seasonal and highly structured aerosol formation from precursor, tropospheric source gases (Vernier et al., 2011a; Neely et al., 2014; Thomason and Vernier, 2013).

Many of the studies mentioned above have involved the use of Cloud Aerosol Lidar and Infrared Pathfinder Satellite Observation (CALIPSO) space-borne lidar measurements (Winker et al., 2007), which nominally measures backscatter profiles approximately every 300 m along track with approximately 200 m vertical resolution. However, the stratospheric backscatter signal is weak and requires averaging of only the night time measurements over several days and typically 0.5 km vertically and 500 km horizontally (Vernier et al., 2011b). Additionally, the uncertainty in the calibration with respect to the molecular background that is on the order of the stratospheric aerosol signal leads to a potential bias in the stratospheric measurements (Rogers et al., 2011). CALIPSO was launched in 2006 and although it is presently still operational, it is also operating beyond its design lifetime. [More recently the lidar instrument Cloud Aerosol Transport System \(CATS\) \(Chuang et al., 2013\) has been placed on the international space station in 2015 for an expected mission lifetime of three years.](#)

Continued stratospheric aerosol observations from space are drastically needed though few, if any, planned missions with such capability are underway. In this paper we present the design and test of a prototype instrument for potential future satellite-based stratospheric aerosol observation. The Aerosol Limb Imager (ALI) concept is a relatively small, low-cost, low-power, passive instrument, suitable for microsatellite deployment, with the capability to provide high spatial resolution measurements, both vertically and horizontally, of the visible/NIR aerosol extinction coefficient. The basic idea is to leverage the clear advan-

tages of the limb scatter technique as a passive, and therefore low mass and power, means to obtain daily global coverage, with a two dimensional hyperspectral imager for filling cross-track observation.

The ALI instrument concept is built around the use of an Acousto-Optic Tunable Filter (AOTF), which is a novel filtering technology that provides the ability to rapidly select the central wavelength of an image with no moving parts. These filters, which have recently been developed as large aperture, imaging quality devices, operate very efficiently in the red and near infrared spectral range, which is a well matched spectral range for limb scatter sensitivity to aerosol and cloud (Rieger et al., 2014). Additionally, the spectral bandpass of the AOTF, which is typically between 3–6 nm at these wavelengths, is very suitable for the broadband scattering characteristics of the aerosol limb signal. The two dimensional imaging nature of the design provides the capability to achieve at least sub-kilometer resolution at the tangent point, which is on the order of the scale size of the upper troposphere and lower stratosphere (UTLS) aerosol features mentioned above.

It should be noted that the basic instrument design concept of ALI is very similar to that of the Atmospheric Limb Tracker for the Investigation of the Upcoming Stratosphere (ALTIUS) (Dekemper et al., 2012), which is a Belgian instrument concept from the Belgian Institute for Space Aeronomy (BIRA). ALTIUS is designed to measure limb scattered sunlight; however, it also has solar, stellar, and planetary occultation modes and is scientifically focused on trace gas measurements, particularly for ozone, whereas ALI is optimized for aerosol observation.

## 2 ALI instrument design

ALI is a simple optical system that images essentially a single wavelength at a time through the use of an acousto-optic tunable filter (AOTF). The AOTF is a unique device that allows for the filtering without any moving parts and relatively low power consumption. However, the AOTF operation requires important instrument design considerations to account for its optical operation. For example, the diffractive qualities of the AOTF depend on the angle that light enters the device. Additionally, in practice the AOTF output is limited to a single linear polarization, which reduces the system throughput and causes potential internal stray light in the system through the rejection of the other linear polarization. The following sections provide a brief introduction to the physical operation of the AOTF, considerations for implementation in a system designed specifically for aerosol, and an overview of the final ALI optical design.

### 2.1 Acousto-optical tunable filter

The primary filtering device behind ALI and the technology that allows for the two dimensional spatial imaging is the AOTF, which is typically made from a birefringent crystal. A radio frequency (RF) wave is propagated through the crystal, and forms an acoustic standing wave that interacts with an incoming beam of light in an effect similar to the diffraction of a specific wavelength. The use of an AOTF for an imaging system has several distinct advantages due to its low mass, fast stabilization times of a few microseconds, and no moving parts. Although many applications use small, non-imaging AOTFs with various configurations, large aperture, birefringent, non-collinear acousto-optic devices are typically used in imaging systems. A non-collinear device is one where the input light beam and the RF acoustic wave are not aligned. Thanks to recent advancements in

non-collinear AOTF technology these devices now have relatively high efficiency and robust imaging quality (Georgiev et al., 2002; Voloshinov et al., 2007).

To create the diffraction of a specific wavelength, a momentum matching criterion must be held where the wave vectors of the acoustic wave match the difference of the incoming and diffracted light wave vectors as seen in Fig. 1. This condition is known as the Bragg matching criterion and is given by

$$\mathbf{k}_i = \mathbf{\kappa} + \mathbf{k}_d \quad (1)$$

where  $|\mathbf{k}_i| = 2\pi n_i/\lambda$  is the wave number of the incident light,  $|\mathbf{k}_d| = 2\pi n_d/\lambda$  is the wave number of the diffracted light, and  $|\mathbf{\kappa}| = 2\pi F/\nu$  is the wave number of the ~~aeousto~~-acoustic wave. The parameters  $\lambda$ ,  $F$  and  $\nu$  are the wavelength of light in vacuum, the frequency of the RF wave, and the phase velocity in the crystal respectively and the indices of refraction for the incident and diffracted light are  $n_i$  and  $n_d$  respectively. Using the condition given in Eq. (1) and the wave vector diagram gives the following relation for a birefringent material undergoing Bragg diffraction

$$\lambda = \frac{\Delta n \nu \sin^2(\theta_i + \alpha)}{F \sin \theta_i} \quad (2)$$

where  $\Delta n$  is the absolute difference between the ordinary and extraordinary indices of refraction,  $\theta_i$  is the angle of incidence of the incoming light, and  $\alpha$  is the angle the acoustic wave propagates through the device (Voloshinov and Mosquera, 2006).

Note that the wavelength diffracted by the AOTF is inversely related to frequency of the RF wave. This equation also displays an important implication of the operation of the device that affects the design possibilities in an imaging system. That is, the wavelength of diffracted signal is dependent on the angle of incidence of the incoming wave. Therefore, passing the light beam through the AOTF at different incident angles will result in slightly different outgoing diffracted wavelengths. Also, through the described interaction, the diffracted light goes through a  $90^\circ$  rotation in polarization (Voloshinov, 1996).

For ALI prototyping purposes, a  $10\text{mm} \times 10\text{mm}$  aperture imaging quality ~~ATOF~~-AOTF was acquired from Brimrose of America (model number TEAFI10-0.6-1.0-MSD) with a Gooch and Housego driver (model number 64020-200-2ADMDFS-A). The AOTF is optically tuned for the wavelength octave of 600 to 1200 nm, corresponding to an RF range of 156 to 70 MHz. It is made from tellurium dioxide ( $\text{TeO}_2$ ), a birefringent crystal with indices of refraction at 800 nm of 2.226 and 2.373 for the ordinary and extraordinary modes respectively (Uchida, 1971). The acousto-optic diffraction angle ~~is not constant angle with~~ ~~wavelength varies as the filtered wavelength is changed~~, so in order to achieve an essentially constant diffraction angle the rear surface of the crystal is cut at a specific angle, such that the refraction at this final surface compensates for the angular change with wavelength. For our specific sample, the diffracted extraordinary light beam is compensated in this way and is diffracted  $2.7^\circ$  from the input optical axis of the device. The ordinary light beam also undergoes diffraction, but at a non-constant angle from the optical axis with respect to wavelength and is not imaged by the system. A schematic of the basic light paths through the AOTF is shown in Fig. 2a.

## 2.2 Instrument design

The ALI prototype that we have developed has been designed specifically for testing from a stratospheric balloon at a float altitude of approximately 35 km. In this geometry, a field of view that captures a vertical image of the limb from the horizontal at float down to the tangent line to the surface corresponds to  $6^\circ$  (Fig. 3). This is substantially larger than similar imaging requirements from low earth orbit, where the same tangent altitude range would be covered by about a one degree field of view. The target vertical resolution of the measured radiance profiles is 200 m in tangent altitude. A wavelength range of 600–1000 nm was decided upon for the prototype, mostly to align well with the spectral response of a standard and readily available CCD detector. We ~~also attempted to pay~~ paid careful attention to stray light reduction including both internal scatter and out-of-field signal.

The use of the AOTF essentially limits the optical design to two possible basic layouts: the telecentric or the telescopic system. The telecentric system uses a layout that removes perspective from the image and object plane and the telescopic system uses a telescope as the front end optics. This limitation is mainly that the incoming light beams at the AOTF device must enter at less than the acceptance angle, which is defined by a threshold beyond which the diffraction efficiency falls off sharply. These AOTF layouts have been studied previously (Suhre et al., 2004); however they are briefly explained here in the context of our intended purpose of limb imaging aerosol. The upshot is that the telescopic, or afocal, system causes a wavelength gradient to be formed across the image plane, whereas the telecentric design overcomes this problem but has a larger spectral point spread function, and a slight change in focus with wavelength. The optical design software Code V was used to assist in designing and analyzing the performance of both of the optical layouts.

A telecentric layout leads to focused light bundles passing through the AOTF. The filtered image then has a constant wavelength across the entire image with a larger spectral point spread function, since the diffracted wavelength is dependent on incident angle, as seen in Eq. (2). This layout has two inherent issues. First, it is sensitive to any surface defects of the crystal since the light path is focused very near the AOTF surfaces. Second, a shift in the location of the imaging focal plane occurs that is dependent on wavelength such that perfect focus can only be obtained for a single wavelength. Defocusing will occur at the image plane for all other wavelengths and in order to correct for this problem additional compensating optics would need to be added or the detector would need to be actively moved as the wavelengths are scanned.

In the telescopic layout, collimated light for each line-of-sight passes through the AOTF. This results in a few fundamental differences that both improve and degrade the imaging quality. First, the light passing through the AOTF from a single line-of-sight enters the AOTF at the same angle, so the image will have a narrower spectral point spread function than the telecentric counterpart. However, each line-of-sight will be diffracted with a different fundamental central wavelength due to the angular dependence in the AOTF diffraction (Eq. 2). The scanned spectrum then has better spectral resolution than obtained with the telecentric system, but there will be a wavelength gradient radiating out from the center of the image. Second, since light in this design passes through the AOTF collimated, the focal point of the image no longer changes with wavelength. Instead, a lateral displacement of each line-of-sight occurs based on the angle of incidence and the diffracted wavelength which causes a slight

change in magnification of the final image. The lateral displacement that occurs is given by the following relation

$$\delta = (n(\lambda) - 1) \frac{t\theta}{n(\lambda)} \quad (3)$$

where  $\delta$  is the displacement from the original path and  $t$  is the thickness of the crystal. However, it turns out that this wavelength dependent change is negligible-less than a micron for the current ALI design and is considered negligible.

5 In light of the requirements for imaging aerosol, we have chosen a telescopic design for the ALI prototype. Since the wavelength gradient across the image is small compared to the slowly varying aerosol scattering cross section, the fixed image plane is preferable for the improvement it provides in spatial imaging, particularly as we desired to use as simple as possible an optical design.

We used a very simple three lens optical layout with commercial off-the-shelf components. Two lenses before the AOTF  
10 form a simple telescope for the Front End Optics (FEO), and a single focusing lens behind the AOTF comprises the Back End Optics (BEO). The AOTF is oriented such that the detected image is formed from the diffracted beam of the vertically polarized, i.e. extraordinary, light (defined at the entrance aperture). A linear polarizer with an extinction ratio greater than  $10^{-5}$   
5 is placed at the back of the FEO to remove the incoming horizontal, or ordinary, polarized beam. The diffracted extraordinary beam undergoes a  $90^\circ$  rotation in polarization so a second linear polarizer, oriented at  $90^\circ$  to the first, is used after the AOTF  
15 and before the BEO to remove the undiffracted beam. This is shown schematically in Fig. 2b. Note that even with the high extinction ratio of the polarizers, a not insignificant fraction of light that is intended to be blocked passes through the system. The diffracted extraordinary signal compresses-comprises at most a  $\sim 10$  nm bandpass fraction of one polarization such that the unabsorbed broadband signal from the polarizers can be on the same order of intensity as the diffracted signal.

The extraordinary diffracted light is  $2.7^\circ$  from the optical axis and to compensate, the entire optical chain after the AOTF  
20 is mechanically aligned with this direction. The BEO forms the image of the signal on a QSI 616s 16 bit CCD with 1536 by 1024 pixels. A ray tracing diagram for ALI's optical system was created using the CODE V optical design software and can be seen in Fig. 4. No corrections were attempted to reduce chromatic or spherical aberrations within the system and the system exhibits some coma due the large field of view and the curvature of the lenses near the edge of the field of view. Analysis with Code V shows that the distortion due to these effects across the center two degrees of the field of view is a change of less  
25 than 1 % change across the entire wavelength range. The final one degree shows a distortion of less than 4 %. An analysis was also performed to determine the minimum resolution required to achieve a Modular Transfer Function (MTF) of 0.3 across the entire field of view for all wavelengths (Smith, 2000). To obtain the MTF across the entire field of view a 7 pixel running average is required. This translates to an average vertical and horizontal resolution of 210 m across the entire ALI field of view at the tangent point. A tolerance study was also performed with Code V to assess the capability of the system within the  
30 tolerances of the mounting equipment and was found that the system was insensitive to tilts and offsets within the system.

The SASKTAN-HR (Bourassa et al., 2008; Zawada et al., 2015) radiative transfer model was used to assist in determining exposure times and entrance pupil of ALI. This was performed by using ground-based sky measurements during a cloudless day at an azimuth of  $90^\circ$  from the sun at a variety of exposure times (0.01 to 60 s) and wavelengths (600 to 1000 nm). The sky measurements were used to estimate typical exposure times. The SASKTRAN-HR model was used to compute the ratio of



the modeled radiances from a balloon flight geometry to the ground-based geometry to scale the ground-based exposure times to those for balloon flight. The ALI entrance pupil was selected at 9.91 mm to yield flight exposure times on the order of 1 s. A summary of the optical specification for the ALI prototype is given in Table 1.

5 A long standing concern in the design of limb scatter instruments is the effective rejection of out-of-field stray light. This is due to the bright surface very near to the targeted limb in combination with the exponentially dropping limb signal with tangent altitude. For ALI test observations from the stratospheric balloon, a front end baffle was incorporated. This was designed to minimize the percentage of out-of-field light that can reach the aperture without encountering at least three baffle surfaces. To further reduce the unwanted signal, each baffle maintains a height to pitch ratio greater than 0.5 (Fischer et al., 2008). The baffle is 300 mm long with a cross section of 70 mm  $\times$  70 mm and contains seven veins spaced throughout the length. The  
10 effectiveness of the baffle was measured against that of a simple aperture through laboratory testing yielding an approximately 8 fold decrease in measured out-of-field stray light.

A SolidWorks rendition of the completed ALI prototype is shown in Fig. 5. The base plate of the instrument is tilted at 3° from the horizontal so the complete 6° vertical field of view spans from the tangent point to the ground to the float altitude once mounted on the level balloon gondola. With the simple off-the-shelf optics the operating temperature of ALI during the  
15 mission was not actively controlled, although the instrument temperature is monitored in several locations along the optical chain and at the detector for later analysis. A simple covering of insulating foam with a reflective coating was used to reduce temperature extremes due to the cold ambient environment and direct solar heating.

Software and controlling hardware for the instrument was developed for autonomous or commanded control during the balloon flight. A Debian Linux operating system with C++ based software controls the hardware and science data collection  
20 operation. The onboard computer is a VersaLogic PC-104 OCELOT computer with fanless operation and a thermal operating range of −40 to 85 °C. The onboard system provides two-way communication to a ground based station through UDP protocol and sends data, including images and housekeeping information, to the ground, as well as receives commands from ground control.

It should be noted that our choice of a telescopic optical layout for ALI is actually the opposite choice of that made for  
25 the ALTIUS design, which uses a telecentric optical layout. For that instrument, the need for spectral resolution for trace gas retrieval makes the decision to use telecentric optics quite clear (Dekemper et al., 2012). Given that basic design difference, the overall optical specifications are quite similar between the ALI and ALITUS prototype instruments (again see Table 1 for ALI specifications), although two key differences are noted. First, by using a telescopic layout the maximum field of view for ALI is determined by choosing lenses to ensure light enters ALI within the acceptance angle of the AOTF. This allows  
30 for a larger possible field of view than with a telecentric system where the field view is defined by the aperture of the AOTF. Second, the f-number for ALTIUS is 14.32 compared to 7.5 for ALI, which allows ALI to increase light throughput at the cost of slightly higher aberrations in the final image. Dekemper et al. (2012) [reports-report](#) that the visible channel of ALTIUS was breadboarded and tested by taking ground based measurements of a smoke stack plume. They used the measurements to retrieve NO<sub>2</sub> slant column density using 10 s exposure times; although, they note that an increase in measurement frequency



would improve the instrument capabilities. This also factored into our decision to use telescopic optics to increase throughput for ALI.

### 3 Calibration

A series of pre-flight laboratory calibrations were performed in two stages. First, the AOTF was characterized to calibrate it with respect to wavelength registration and spectral point spread function. Secondly, the instrument was characterized as a complete system to provide calibrated radiance. The following calibration measurements were performed on ALI:

- AOTF wavelength calibration
- AOTF point spread function and diffraction efficiency
- stray light calibration
- 10 – flat-fielding correction

#### 3.1 AOTF wavelength calibration

The relationship between the applied acoustic wave frequency and the diffracted wavelength, which is known as the tuning curve defines the wavelength registration to the RF wave of the collected images. This was determined in the laboratory setting by filling the AOTF aperture with collimated light and observing the diffracted, or filtered, signal with a HORIBA iHR320 spectrometer and Synapse 354 308  $1024 \times 256$  pixel CCD. The grating used with the spectrometer had a spectral resolution of 1.2 nm, which is ~~much~~ less than the factory specified resolution of the ~~AOTF~~AOTF. Images were taken at a constant exposure time at a set of acoustic wave radio frequencies spaced every 150 kHz from 75 to 160 MHz. This corresponds to approximately one image every 1 nm. A typical spectrum recorded with the iHR320 is shown in Fig. 6a. The fringes that are visible in the spectrum in Fig. 6a are a known acousto-optic effect (Xu and Stroud, 1992) and for ALI amount to 8 to 14 % of the total signal depending on wavelength and incident angle. The maximum value of each image is then taken to be the central wavelength at each respective acoustic wave frequency.

These central wavelengths for the full set of spectra were empirically found to follow a power function of the form

$$F = a\lambda^{b+c \log \lambda}. \quad (4)$$

The fit of the data to this function form agrees to less than 0.1 % throughout the whole wavelength range such that the final tuning curve was as determined as

$$F = \exp(19.793) \lambda^{-3.381+0.168 \log \lambda} \quad (5)$$

where  $\lambda$  is in nanometers and  $F$  is in MHz with a 0.1 % error in the central wavelength (see Fig. 6b). It should be noted that even though the AOTF optical range is 600 to 1200 nm our analysis only measured wavelengths from 600 to 1080 nm due to the low quantum efficiency of the CCD beyond this range.

### 3.2 AOTF point spread function and diffraction efficiency

The spectral point spread function and diffraction efficiency of the AOTF were also determined in a similar fashion. The same set of experimental data that was used for the wavelength registration was used to find the spectral point spread function by finding the full width at half maximum for each obtained spectrum. These range from 2–5 nm, increasing monotonically with wavelength, and are shown in Fig. 6c. This spectral resolution is well within the specification required in order to retrieve aerosol information as the aerosol scattering cross varies relatively slowly across the visible and near infrared spectral range.

The same set of experimental data was also used to determine the diffraction efficiency of the AOTF, along with an additional measurement of the intensity of the incident collimated light beam. This was simply acquired by removing the AOTF from the same experimental setup. The incident light source was then measured with the iHR320 spectrometer and Synapse CCD. By taking the ratio of the intensity at the diffracted wavelength to the incident intensity the diffraction efficiency was determined. It was found to vary between 54–64 % across the measured spectral range. It should be noted that the diffraction efficiency changes also with respect to incoming angle and this experimental determination only measured the diffraction efficiency at normal incidence (Xu and Stroud, 1992).

### 3.3 Stray light

A laboratory experiment to characterize the stray light in the ALI system was also performed. Two types of stray light exist; the first is out-of-field stray light, i.e. signal that enters the optical path that originates outside of the field of view. The second is internal stray light, which is caused by scattering, reflections or other imperfections in the optical elements. As mentioned above, stray light removal is quite critical for limb scatter measurements.

The use of the AOTF has potential to increase the amount of internal stray light due to the fact that the undiffracted beam and the unmeasured polarization also propagate through the system. However, the diffraction interaction only occurs when the acoustic wave signal is applied, so without the acoustic wave the recorded measurement only contains the stray light in the system. Using this characteristic, the stray light of the system was measured in the laboratory. A 250 W quartz-tungsten light source was passed through a dispersing screen and onto the entrance aperture of ALI, effectively filling the entire aperture and all angles within the field of view. Using a variety of exposure times, ranging from 0.1 to 60s and wavelengths from 650 to 950 nm in 25 nm intervals, this diffuse source was imaged twice; once with the AOTF in its off state, with no driving acoustic wave, and once with the ~~AOTF~~-AOTF in its on state, with the acoustic wave applied (see Fig. 2c). For each pair of measurements the image with the “AOTF-off” only contains stray light in the system, and the “AOTF-on” image contains the stray light combined with the image of the diffuse source. Subtracting the “AOTF-off” image from the “AOTF-on” image yields a final image that contains only the image of the diffuse source. A typical example of a resulting image is shown in Fig. 7. The observed vignetting is caused by the aperture of the AOTF and is expected from the ray trace model. Note that this method also removes any dark current associated with the detector. This two-image method was used operationally during the balloon measurement campaign such that images captured had a corresponding “AOTF-off” image immediately obtained with the same exposure time. For the calibration images an average signal to noise ratio of 40 was noted.

### 3.4 Relative flat fielding calibration

The flat-field calibration corrects optical and detector level differences in the system across the field of view such that a calibrated image of a perfectly diffuse source yields a constant value across the image. The resulting images from the diffuse source described above were used to determine the flat fielding corrections for ALI. These were determined in two steps: spatial and spectral. First, for the spatial correction, for each image at a given wavelength, each pixel was scaled to the mean value of the center  $25 \times 25$  pixels, which had no more than a 4 % standard deviation. ALI is most sensitive at 775 nm so this wavelength was chosen as the reference wavelength of a relative spectral calibration. All flat-fielding corrections were then scaled to the blackbody curve of a tungsten halogen bulb normalized to 775 nm assuming an operating temperature of 3300 K for the bulb using a method by Kosch et al. (2003). No absolute calibration was performed due to lack of availability of an appropriately calibrated source.

## 4 Stratospheric balloon flight

### 4.1 Flight conditions and measurement modes

The Canadian Space Agency (CSA) balloon launch base is in Timmins, Ontario (48.47° N, 81.33° W). ALI was integrated onto a CNES pointed gondola and used on-board subsystems, including communications and power. The CNES gondola is an actively pointed gondola with azimuthal pointing precision better than 1' with the use of an onboard star tracker. ALI was orientated so it would be maintained at 90° from the azimuthal direction of the sun, with an overall southern field of view during the mission.

On 19 September 2014 at 05:35 UTC (01:35 LT) ALI was launched as part of the Nimbus 7 mission from the CSA Timmins balloon launch facility. During the launch, the sky was clear with light winds allowing for a safe and uneventful launch. The ascent of the gondola occurred in darkness and reached its flight altitude of 36.5 km at 08:17 UTC. First light was observed by ALI at 09:39 UTC and spectral images were recorded until 14:42 UTC. A visualization of the flight path with major landmarks noted can be found in Fig. 8a. Temperature profiles for the ambient atmosphere and instrument are shown in Fig. 8b. The black curve is the ambient atmospheric temperature at the gondola altitude and location during the flight as obtained from ECMWF reanalysis (Dee et al., 2011).

During the mission, ALI operated in two primary acquisition modes, a calibration mode and an aerosol imaging mode. The first mode, the calibration mode, was primarily used during ascent when the gondola was in the darkness and intermittently between the aerosol mode during sunlit conditions. During this mode the filtering of the AOTF was not enabled and the system imaged essentially only dark current during the ascent in darkness and stray light during sunlit conditions. Eight exposures are taken in the calibration mode with 0.05, 0.1, 0.5, 1, 2, 3, 5, 10 s exposure times. The second operational mode, the aerosol mode, recorded measurements in a cycle that contained 13 pairs of images across the spectral range (650–950 nm every 25 nm), the pairs being a calibration image with the “AOTF-off” and an image of the limb. Each cycle took approximately 12 min with each measurement set taking approximately 45 s to acquire with exposure times varying between 0.5 to 6 s.

## 4.2 Limb measurements

After the successful post-flight recovery of ALI, 216 raw images were obtained and calibrated as detailed in Sect. 3. An example of a calibrated limb image is shown in Fig. 9a. This is image number 208 at 750 nm taken at 13:57 UTC with a solar zenith angle and solar scattering angle of 63 and 98° respectively. The horizontal structure across the images is nicely revealed by calculating the mean radiance profile across the image and then removing it from each profile. This is shown in Fig. 9b, where thin clouds (2 km vertical extent or less) are clearly seen near and below the tropopause level, with substantial variation in tangent altitude across the horizontal field of view. These clouds were also observed from other instruments on board the gondola during the mission (B. Solheim, personal communication, 2014). A brief check on the CALIPSO quick-look plots also shows clouds at a maximum height of approximately 13 km from measurements taken at 08:40 UTC at 47.24° N, 95.25° W, the nearest measurement point to the ALI location and time. Although these images only have a 35 km extent in the horizontal direction, there is also some indication of horizontal variation in radiance significantly above the cloud level, possibly due to real atmospheric variability in the aerosol layer. It should also be noted that some high altitude stray light is also visible in this mean residual image that was not observed in the laboratory tests. This may be due to contamination from scattering from a baffle vein or a nearby component of the gondola, although the true cause is unknown at this point.

For ease of further analysis, and to increase the precision of the measurements to a minimum of 0.6 MTF the images were averaged into cells of 25 pixels horizontally, and averaged vertically onto a 1 km tangent altitude grid. The radiance profiles from the center column of the images for all measurements obtained during the flight are shown in Fig. 10. The first sets of profiles, the dashed lines, which start near zero and move toward larger values, are the measurements that were recorded near and during sunrise so the gradual increase is therefore expected. Measurements obtained for solar zenith angles less than 90° are represented by the solid lines. These radiance profiles follow a similar, and expected exponential shape, with some variability at tangent altitudes below 12 km corresponding largely to changing cloud conditions.

A full cycle of 13 spectral images (numbers 204–216) were used in Fig. 11 to show the spectrum of relative calibrated radiances at selected tangent altitudes. The estimated uncertainty in the radiance is represented by the shading. The uncertainty is approximately five percent from 5 to 20 km and increases up to eight percent from 20 to 35 km. The error term includes the CCD read, DC offset, dark current, stray light removal, and flat fielding correction error terms. The spectra displays the expected and relatively smooth fall off in intensity with increasing wavelength with Chappuis ozone absorption seen at the lower wavelengths; however, the reason for the peak in the spectra at 875 nm is not known and may be due to an inconsistency in the pre-flight calibration.

## 4.3 Retrieval methodology

As a first application of the ALI measurements, we have applied a slightly modified version of the standard OSIRIS stratospheric aerosol extinction retrieval (Bourassa et al., 2012b) to the flight measurements. This inversion algorithm, which is applied from the tropopause to 30 km altitude, assumes log-normally distributed hydrated sulphuric acid droplets in order to calculate the aerosol scattering cross sections from the Mie scattering solution (Wiscombe, 1980). The modeled radiances for

the nonlinear inversion were computed with the SASKTRAN High Resolution radiative transfer engine (SASKTRAN-HR) (Bourassa et al., 2008; Zawada et al., 2015) using the newly developed vector module for polarization (Dueck et al., 2015). The output of SASKTRAN-HR gives the Stokes vectors for the radiance on the model reference frame, which are then rotated into the instrument's coordinate system. Once rotated, the polarization signal required to match the ALI measurement is the vertical polarization given by

$$I_v = \frac{1}{2} (I - Q) \quad (6)$$

where  $I$  and  $Q$  are Stokes parameters defined by  $I = \langle E_x^2 \rangle + \langle E_y^2 \rangle$  and  $Q = \langle E_x^2 \rangle - \langle E_y^2 \rangle$ . The variables  $E_x$  and  $E_y$  are the horizontal and vertical component of the electric field in the instrument reference frame.

The relative radiance measurements from ALI are used to create measurement vectors,  $\mathbf{y}$ , as specified in Bourassa et al. (2012b) in the form,

$$\mathbf{y} = \log \left( \frac{I_v(z, \lambda)}{I_v(z_{\text{ref}}, \lambda)} \right) - \log \left( \frac{\frac{I_{v, \text{rayleigh}}(z, \lambda)}{I_{v, \text{rayleigh}}(z_{\text{ref}}, \lambda)} \frac{I_{v, \text{rayleigh, model}}(z, \lambda)}{I_{v, \text{rayleigh, model}}(z_{\text{ref}}, \lambda)}}{\frac{I_{v, \text{rayleigh}}(z_{\text{ref}}, \lambda)}{I_{v, \text{rayleigh, model}}(z_{\text{ref}}, \lambda)}} \right) \quad (7)$$

where  $I_v(z, \lambda)$  is the measured relative radiance from ALI and  $I_v(z_{\text{ref}}, \lambda)$  is the relative radiance at a high reference tangent altitude where there is little aerosol contribution. For the ALI measurements, the highest possible tangent altitude where the signal is above the noise threshold is approximately 30 km tangent height and typical values for  $z_{\text{ref}}$  were between 27 and 30 km. The second term in Eq. (7) uses modeled radiances from SASKTRAN-HR with only the molecular atmosphere to approximately remove the Rayleigh signal. This is done to improve the speed of the convergence of the retrieval (Bourassa et al., 2012b). An initial guess state,  $\mathbf{x}$ , for the aerosol extinction and an assumed particle size distribution profile are set in the SASKTRAN-HR model. The forward model vector is then constructed similarly to the measurement vector, and used in combination with the measurement vector to update the aerosol extinction coefficient profile using Multiplicative Algebraic Reconstruction Technique (MART) algorithm,

$$x_i^{n+1} = x_i^n \sum_j \frac{y_j}{F(z_j)} W_{ij} \quad (8)$$

where  $x_i$  is the aerosol extinction at each model altitude,  $i$  and  $j$  denotes a tangent altitude from the measurements.  $W_{ij}$  is an element of the weighting matrix that relates the importance of each element of the measurement vector to each shell altitude. This method described in detail by Bourassa et al. (2007).

Once a retrieval has been completed for a measured radiance profile, the result is then used to estimate the error in the retrieved extinction. For each altitude, a gain matrix,  $\mathbf{G}$ , is calculated through successive numerical perturbation of the measurement vector and re-retrieval (Rodgers, 2000). A much faster method to use the Jacobian to determine the error has been performed (Bourassa et al., 2012a) but makes an assumption that the gain matrix is equal to the inverse of the Jacobian, as typically the averaging kernel is close to the identity matrix. However, this method adds additional uncertainty to the error estimate and with a limited set of balloon data, it is possible to calculate the gain matrix directly. The error at each retrieved

altitude is then given by

$$\mathbf{E} = \mathbf{G}\mathbf{S}_e\mathbf{G}^T \quad (9)$$

where  $\mathbf{S}_e$  is the covariance matrix of the measurement vector and  $\mathbf{E}$  is the covariance of the retrieved aerosol profile (Rodgers, 2000). The reported precision for ALI aerosol extinction retrievals is the square root of the diagonal of  $\mathbf{E}$ .

- 5 Using the retrieved extinction profiles for the complete spectral range, we have attempted a determination of the Angström exponent using a method similar to that outlined by Rault and Loughman (2013) for the OMPS-LP analysis. In this method, the independently retrieved extinction profiles at each wavelength and altitude are fit with a straight line in log-wavelength, log-extinction space. The slope of this line corresponds to the ~~Angstrom~~-Angström exponent. This is then used to find the best match to the spectral dependence of the Mie scattering cross section in order to update the particle size distribution. With  
10 only one piece of information, the mode-width of the log-normal distribution is fixed to 1.6 and the mode radius is updated. The extinction retrievals are then performed again at each wavelength and the process is iterated until the ~~Angstrom~~-Angström exponent, corresponding to the determined mode radius, converges.

- Ideally, the ALI measurements would be used independently to also retrieve ozone in the Chappuis band. However, due to the spectral range of the prototype, only a small fraction of the long wavelength side of the absorption band was captured. For  
15 this analysis, we have not retrieved the ozone profile but have set the ozone profile in SASKTRAN-HR to an average of the five closest coincident ozone profiles measured by OSIRIS at the ALI location and time. The surface albedo used is also from the OSIRIS scans since the two instruments share a similar measurement method and should determine a similar albedo for the cloudy conditions. Preferably albedo would be determined from the ALI following the method of Bourassa et al. (2012b), however due to the lack of an absolute calibration this was not possible.

## 20 4.4 Results

- The above retrieval method was applied to a complete cycle of ALI spectral images (number 204–216 of the balloon mission). The retrieved aerosol extinction profiles can be seen in the left panel of Fig. 12. Note the log scale. ~~After the retrieval, the~~ The difference between the measurement and forward model vectors were less than 2 % for the majority of the retrieval region, approximately 13 to 28 km, across all wavelengths. Note the behavior of decreasing extinction with increasing wavelength as  
25 expected due to the dependence of the cross section with respect to particle size.

- The ALI 750 nm aerosol extinction profile is shown in the right panel of Fig. 12 in blue with the shading representing the precision of the retrieval. The error is strictly based on measurement error and neglects any model and atmospheric state errors. The ~~green-red~~ curve is the average 750 nm aerosol extinction profiles of the same five coincident OSIRIS scans used for the ozone profile. The retrieved extinction profiles from ALI and OSIRIS are within with the total retrieval uncertainty ~~below 20-~~  
30 ~~It is encouraging, however, that the instruments follow the same overall profile shape including the stratospheric layer and the steep increase below 15. However, the OSIRIS and ALI extinctions do not agree within error between 20 to 25.~~ Aerosol is notoriously difficult to validate in remote sensing with various technique and instrument geometries, and yet the SAGE II, SAGE III and OSIRIS differences are generally below 20–30 % up to 30 km (Bourassa et al., 2012b; Rieger et al., 2015) ~~so~~

the disagreement between OSIRIS and ALI from 20 to 25 found here is somewhat puzzling. However, given the retrieved uncertainty, the OSIRIS profile is only outside the upper error bound of ALI by less than 10 %. There are also several possible systematic errors not accounted for in the inversion including the choice of retrieval altitude ranges, particle size composition and distributions, distribution and particle composition, stray light, and the high altitude aerosol load. This is also the first polarized limb scatter retrieval to our knowledge and so. The solar scattering angle for a measurement can also have an effect on the retrieved profile due sensitivity to the scatter cross sections from the particle size distributions. For the ALI image the solar scattering angle is 98 degrees and for the five OSIRIS scan they are 77, 89, 90, 91, 92, 93 degrees. With the exception of the forward scatter angles of 77 and 89 degrees from OSIRIS the scatter angles between OSIRIS and ALI are similar and should not cause a large effect on the retrieved profiles. Furthermore, there may be further issues to explore with the polarized measurement and forward model. Regardless, the results are encouraging.

The particle size method outlined above was also applied to this measurement set. The retrieved extinction at a given altitude was rejected from the straight line fit if the converged forward model radiance at that altitude was not within 2 % of the measurement vector. In the case shown in Fig. 13, at the 14.5 km altitude point, only 10 of the 13 possible wavelengths contributed to the determination of the Angström exponent. The first panel of Fig. 13 shows the median Angström exponent that was determined after each iteration and convergence can be seen after a couple iterations. The results are shown in the second panel of Fig. 13, where the Angström exponent is between 2 and 3 throughout the altitude range from 13 to 22 km. Assuming a mode width of 1.6 yields a median mode radius of  $0.077 \mu\text{m}$  or Angström coefficient of 2.7. In comparison to typical levels of background aerosol from the Laramie, Wyoming OPC data (Deshler et al., 2003) the retrieved particle size parameters are certainly within an expected range (Angström coefficient of 2.1-3.4), although there is a relatively large error bar on the retrieved value, limiting the usefulness of the retrieved particle size information for background aerosol. However, with these error bars, even this limited spectral range would have the sensitivity to detected particle size changes as seen by OSIRIS and SAGE II over recent decades due to small volcanic perturbations (Rieger et al., 2014).

## 5 Conclusions

The ALI prototype, which is telescopic acousto-optic imager, has been used to successfully measure two dimensional spectral images of the atmospheric limb from stratospheric balloon. The observed radiances appear to be of high quality and show both vertical and horizontal features of the cloud and aerosol layers. Aerosol extinction coefficient profiles were retrieved from the ALI data that show reasonable agreement with OSIRIS satellite measurements.

No large scale issues were found with the instrument performance; however, some future changes would be recommended. First, an absolute calibration of the instrument would allow ALI to determine the effect albedo directly, as is done with OSIRIS. This would remove some of the uncertainty in the model inputs and likely yield higher quality results. This is simply a matter of having access to the calibration equipment. Also, even with the baffle and the robust method of removing stray light with the cycling of the AOTF, some stray light was still observed in the obtained images. Impact and mitigation of this should be tackled in future iterations of the instrument.



*Acknowledgements.* This work would have not been possible without funding from the CSA to design and build ALI through the FAST program as well as the CSA building and managing the launch facility in Timmins, Ontario. Also, thanks to CNES for funding and overseeing the launches at Timmins in 2014. The optical design analysis was performed in thanks to Synopsys for the use of a Code V software license. The CALIPSO data were obtained from the NASA Langley Research Center Atmospheric Science Data Center. As well, thanks to Nick

5 Lloyd for help in development of the flight code, without his efforts this work would have not been accomplished.

## References

- Andersson, S. M., Martinsson, B. G., Vernier, J.-P., Friberg, J., Brenninkmeijer, C. A., Hermann, M., van Velthoven, P. F., and Zahn, A.: Significant radiative impact of volcanic aerosol in the lowermost stratosphere, *Nature*, 6, 7692, doi:10.1038/ncomms8692, 2015.
- Beuttell, R. G. and Brewer, A. W.: Instruments for the measurement of the visual range, *J. Sci. Instrum.*, 26, 357–359, doi:10.1088/0950-5767/26/11/302, 1949.
- Bourassa, A. E., Degenstein, D. A., Gattinger, R. L., and Llewellyn, E. J.: Stratospheric aerosol retrieval with optical spectrograph and infrared imaging system limb scatter measurements, *J. Geophys. Res.*, 112, D10217, doi:10.1029/2006JD008079, 2007.
- Bourassa, A. E., Degenstein, D. A., and Llewellyn, E. J.: SASKTRAN: a spherical geometry radiative transfer code for efficient estimation of limb scattered sunlight, *J. Quant. Spectrosc. Ra.*, 109, 52–73, doi:10.1016/j.jqsrt.2007.07.007, 2008.
- 10 Bourassa, A. E., McLinden, C. A., Bathgate, A. F., Elash, B. J., and Degenstein, D. A.: Precision estimate for Odin-OSIRIS limb scatter retrievals, *J. Geophys. Res.*, 117, D04303, doi:10.1029/2011JD016976, 2012a.
- Bourassa, A. E., Rieger, L. A., Lloyd, N. D., and Degenstein, D. A.: Odin-OSIRIS stratospheric aerosol data product and SAGE III inter-comparison, *Atmos. Chem. Phys.*, 12, 605–614, doi:10.5194/acp-12-605-2012, 2012b.
- Bourassa, A. E., Robock, A., Randel, W. J., Deshler, T., Rieger, L. A., Lloyd, N. D., Llewellyn, E. T., and Degenstein, D. A.: Large volcanic aerosol load in the stratosphere linked to Asian monsoon transport, *Science*, 337, 78–81, 2012c.
- 15 Bourassa, A. E., Robock, A., Randel, W. J., Deshler, T., Rieger, L. A., Lloyd, N. D., Llewellyn, E., and Degenstein, D. A.: Response to comments on “Large volcanic aerosol load in the stratosphere linked to Asian monsoon transport”, *Science*, 339, 647–647, 2013.
- Bovensmann, H., Burrows, J., Buchwitz, M., Frerick, J., Noël, S., Rozanov, V., Chance, K., and Goede, A.: SCIAMACHY: mission objectives and measurement modes, *J. Atmos. Sci.*, 56, 127–150, 1999.
- 20 Charlson, R. J., Ahlquist, N., Selvidge, H., and MacCready Jr., P.: Monitoring of atmospheric aerosol parameters with the integrating nephelometer, *JAPCA J. Air Waste Ma.*, 19, 937–942, 1969.
- Chazette, P., David, C., Lefrere, J., Godin, S., Pelon, J., and Mégie, G.: Comparative lidar study of the optical, geometrical, and dynamical properties of stratospheric postvolcanic aerosols, following the eruptions of el chichon and mount pinatubo, *J. Geophys. Res.*, 100, 23–195, 1995.
- 25 [Chuang, T., Burns, P., Walters, E. B., Wysocki, T., Deely, T., Losse, A., Le, K., Drumheller, B., Schum, T., Hart, M., Puffenburger, K., Ziegler, B., and Hovis, F.: "Space-based, multi-wavelength solid-state lasers for NASA's Cloud Aerosol Transport System for International Space Station \(CATS-ISS\). Proc. SPIE, 8599, Solid State Lasers XXII: Technology and Devices, 85990N. doi:10.1117/12.2005545, 2013.](#)
- Cisewski, M., Zawodny, J., Gasbarre, J., Eckman, R., Topiwala, N., Rodriguez-Alvarez, O., Cheek, D., and Hall, S.: The stratospheric aerosol and gas experiment (SAGE III) on the international space station (ISS) mission, *Proc. SPIE*, 9241, 924107–924107-7, doi:10.1117/12.2073131, 2014.
- 30 Clarisse, L., Coheur, P.-F., Theys, N., Hurtmans, D., and Clerbaux, C.: The 2011 Nabro eruption, a SO<sub>2</sub> plume height analysis using IASI measurements, *Atmos. Chem. Phys.*, 14, 3095–3111, doi:10.5194/acp-14-3095-2014, 2014.
- Damadeo, R. P., Zawodny, J. M., Thomason, L. W., and Iyer, N.: SAGE version 7.0 algorithm: application to SAGE II, *Atmos. Meas. Tech.*, 6, 3539–3561, doi:10.5194/amt-6-3539-2013, 2013.
- 35 Dee, D. P., Uppala, S. M., Simmons, A. J., Berrisford, P., Poli, P., Kobayashi, S., Andrae, U., Balmaseda, M. A., Balsamo, G., Bauer, P., Bechtold, P., Beljaars, A. C. M., van de Berg, L., Bidlot, J., Bormann, N., Delsol, C., Dragani, R., Fuentes, M., Geer, A. J., Haimberger, L.,

- Healy, S. B., Hersbach, H., Hlm, E. V., Isaksen, L., Kllberg, P., Khler, M., Matricardi, M., McNally, A. P., Monge-Sanz, B. M., Morcrette, J.-J., Park, B.-K., Peubey, C., de Rosnay, P., Tavalato, C., Thpaut, J.-N., and Vitart, F.: The ERA-interim reanalysis: configuration and performance of the data assimilation system, *Q. J. Roy. Meteor. Soc.*, 137, 553–597, doi:10.1002/qj.828, 2011.
- Dekemper, E., Loodts, N., Opstal, B. V., Maes, J., Vanhellemont, F., Mateshvili, N., Franssens, G., Pieroux, D., Bingen, C., Robert, C.,  
5 Vos, L. D., Aballea, L., and Fussen, D.: Tunable acousto-optic spectral imager for atmospheric composition measurements in the visible spectral domain, *Appl. Optics*, 51, 6259–6267, doi:10.1364/AO.51.006259, 2012.
- Deshler, T., Hervig, M., Hofmann, D., Rosen, J., and Liley, J.: Thirty years of in situ stratospheric aerosol size distribution measurements from Laramie, Wyoming (41 N), using balloon-borne instruments, *J. Geophys. Res.*, 108, 4167, doi:10.1029/2002JD002514, 2003.
- Deshler, T., Anderson-Sprecher, R., Jger, H., Barnes, J., Hofmann, D. J., Clemesha, B., Simonich, D., Osborn, M., Grainger, R. G., and  
10 Godin-Beekmann, S.: Trends in the nonvolcanic component of stratospheric aerosol over the period 1971–2004, *J. Geophys. Res.*, 111, D01201, doi:10.1029/2005JD006089, 2006.
- Dueck, S. R., Bourassa, A. E., and Degenstein, D. A.: Polarization in the SASKTRAN radiative transfer framework, in preparation, 2015.
- Ernst, F., von Savigny, C., Rozanov, A., Rozanov, V., Eichmann, K.-U., Brinkhoff, L. A., Bovensmann, H., and Burrows, J. P.: Global stratospheric aerosol extinction profile retrievals from SCIAMACHY limb-scatter observations, *Atmos. Meas. Tech. Discuss.*, 5, 5993–  
15 6035, doi:10.5194/amtd-5-5993-2012, 2012.
- Fairlie, T. D., Vernier, J.-P., Natarajan, M., and Bedka, K. M.: Dispersion of the Nabro volcanic plume and its relation to the Asian summer monsoon, *Atmos. Chem. Phys.*, 14, 7045–7057, doi:10.5194/acp-14-7045-2014, 2014.
- Fischer, R. E., Tadic-Galeb, B., and Yoder, P. R.: *Optical System Design*, 2nd Edn., McGraw-Hill, New York, USA, 2008.
- Fromm, M., Nedoluha, G., and Charvt, Z.: Comment on “Large volcanic aerosol load in the stratosphere linked to Asian monsoon transport”,  
20 *Science*, 339, p. 647, doi:10.1126/science.1228605, 2013.
- Fromm, M., Kablick, G., Nedoluha, G., Carboni, E., Grainger, R., Campbell, J., and Lewis, J.: Correcting the record of volcanic stratospheric aerosol impact: nabro and sarychev peak, *J. Geophys. Res.*, 119, 10343–10364, doi:10.1002/2014JD021507, 2014.
- Fyfe, J. C., Gillett, N. P., and Zwiers, F. W.: Overestimated global warming over the past 20 years, *Nature Climate Change*, 3, 767–769, 2013.
- 25 Georgiev, G., Glenar, D. A., and Hillman, J. J.: Spectral characterization of acousto-optic filters used in imaging spectroscopy, *Appl. Optics*, 41, 209–217, doi:10.1364/AO.41.000209, 2002.
- Gilbert, K., Turnbull, D., Walker, K., Boone, C., McLeod, S., Butler, M., Skelton, R., Bernath, P., Chateaufneuf, F., and Soucy, M.-A.: The onboard imagers for the Canadian ACE SCISAT-1 mission, *J. Geophys. Res.*, 112, D12207, doi:10.1029/2006JD007714, 2007.
- Haywood, J. M., Jones, A., and Jones, G. S.: The impact of volcanic eruptions in the period 2000–2013 on global mean temperature trends  
30 evaluated in the HadGEM2-ES climate model, *Atmos. Sci. Lett.*, 15, 92–96, doi:10.1002/asl2.471, 2014.
- Hofmann, D., Barnes, J., O’Neill, M., Trudeau, M., and Neely, R.: Increase in background stratospheric aerosol observed with lidar at Mauna Loa observatory and Boulder, Colorado, *Geophys. Res. Lett.*, 36, L15808, doi:10.1029/2009GL039008, 2009.
- Junge, C. E., Chagnon, C. W., and Manson, J. E.: Stratospheric aerosols, *J. Atmos. Sci.*, 18, 81–108, doi:10.1175/1520-0469(1961)018<0081:SA>2.0.CO;2, 1961.
- 35 Kiehl, J. T. and Briegleb, B. P.: The relative roles of sulfate aerosols and greenhouse gases in climate forcing, *Science*, 260, 311–314, doi:10.1126/science.260.5106.311, 1993.
- Kosch, M., Mäkinen, S., Sigernes, F., and Harang, O.: Absolute optical calibration using a simple tungsten light bulb: experiment, in: *Proceedings of the 30th Annual European Meeting on Atmospheric Studies by Optical Methods*, 50–54, 2003.

- Kovilakam, M. and Deshler, T.: On the accuracy of stratospheric aerosol extinction derived from in situ size distribution measurements and surface area density derived from remote SAGE II and HALOE extinction measurements, *J. Geophys. Res.*, 120, 8426–8447, doi:10.1002/2015JD023303, 2015.
- Llewellyn, E., Lloyd, N. D., Degenstein, D. A., Gattinger, R. L., Petelina, S. V., Bourassa, A. E., Wiensz, J. T., Ivanov, E. V., McDade, I. C.,  
5 Solheim, B. H., McConnell, J. C., Haley, C. S., von Savigny, C., Sioris, C. E., McLinden, C. A., Grifoen, E., Kaminski, J., Evans, W. F. J.,  
Puckrin, E., Strong, K., Wehrle, V., Hum, R. H., Kendall, D. J. W., Matsushita, J., Murtagh, D. P., Brohede, S., Stegman, J., Witt, G.,  
Barnes, G., Payne, W. F., Piche, L., Smith, K., Warshaw, G., Deslauniers, D. L., Marchand, P., Richardson, E. H., King, R. A., Wevers, I.,  
McCreath, W., Kyrola, E., Oikarinen, L., Leppelmeier, G. W., Auvinen, H., Megie, G., Hauchecorne, A., Lefevre, F., de La Noe, J.,  
Ricaud, P., Frisk, U., Sjoberg, F., von Scheele, F., and Nordh, L.: The OSIRIS instrument on the Odin spacecraft, *Can. J. Phys.*, 82,  
10 411–422, doi:10.1139/p04-005, 2004.
- McElroy, C. T., Nowlan, C. R., Drummond, J. R., Bernath, P. F., Barton, D. V., Dufour, D. G., Midwinter, C., Hall, R. B., Ogyu, A.,  
Ullberg, A., Wardle, D. I., Kar, J., Zou, J., Nichitiu, F., Boone, C. D., Walker, K. A., and Rowlands, N.: The ACE-MAESTRO instrument  
on SCISAT: description, performance, and preliminary results, *Appl. Optics*, 46, 4341–4356, doi:10.1364/AO.46.004341, 2007.
- Murphy, D. M., Froyd, K. D., Schwarz, J. P., and Wilson, J. C.: Observations of the chemical composition of stratospheric aerosol particles,  
15 *Q. J. Roy. Meteor. Soc.*, 140, 1269–1278, doi:10.1002/qj.2213, 2014.
- Neely, R. R., Yu, P., Rosenlof, K. H., Toon, O. B., Daniel, J. S., Solomon, S., and Miller, H. L.: The contribution of anthropogenic SO<sub>2</sub>  
emissions to the Asian tropopause aerosol layer, *J. Geophys. Res.*, 119, 1571–1579, doi:10.1002/2013JD020578, 2014.
- Rault, D. F. and Loughman, R. P.: The OMPS limb profiler environmental data record algorithm theoretical basis document and expected  
performance, *IEEE T. Geosci. Remote*, 51, 2505–2527, 2013.
- 20 Ridley, D. A., Solomon, S., Barnes, J. E., Burlakov, V. D., Deshler, T., Dolgii, S. I., Herber, A. B., Nagai, T., Neely, R. R., Nevzorov, A. V.,  
Ritter, C., Sakai, T., Santer, B. D., Sato, M., Schmidt, A., Uchino, O., and Vernier, J. P.: Total volcanic stratospheric aerosol optical depths  
and implications for global climate change, *Geophys. Res. Lett.*, 41, 7763–7769, doi:10.1002/2014GL061541, 2014.
- Rieger, L. A., Bourassa, A. E., and Degenstein, D. A.: Stratospheric aerosol particle size information in Odin-OSIRIS limb scatter spectra,  
*Atmos. Meas. Tech.*, 7, 507–522, doi:10.5194/amt-7-507-2014, 2014.
- 25 Rieger, L. A., Bourassa, A. E., and Degenstein, D. A.: Merging the OSIRIS and SAGE II stratospheric aerosol records, *J. Geophys. Res.*,  
120, 8890–8904, doi:10.1002/2015JD023133, 2015.
- Rodgers, C.: *Inverse Methods for Atmospheric Sounding: theory and Practice*, Series on Atmospheric, Oceanic and Planetary Physics: 1999,  
World Scientific, 2000.
- Rogers, R. R., Hostetler, C. A., Hair, J. W., Ferrare, R. A., Liu, Z., Obland, M. D., Harper, D. B., Cook, A. L., Powell, K. A., Vaughan, M. A.,  
30 and Winker, D. M.: Assessment of the CALIPSO Lidar 532 nm attenuated backscatter calibration using the NASA LaRC airborne High  
Spectral Resolution Lidar, *Atmos. Chem. Phys.*, 11, 1295–1311, doi:10.5194/acp-11-1295-2011, 2011.
- Russell, P. and McCormick, M.: SAGE II aerosol data validation and initial data use: an introduction and overview, *J. Geophys. Res.*, 94,  
8335–8338, 1989.
- Sawamura, P., Vernier, J. P., Barnes, J. E., Berko, T. A., Welton, E. J., Alados-Arboledas, L., Navas-Guzmn, F., Pappalardo, G., Mona, L.,  
35 Madonna, F., Lange, D., Sicard, M., Godin-Beekmann, S., Payen, G., Wang, Z., Hu, S., Tripathi, S. N., Cordoba-Jabonero, C., and  
Ho, R. M.: Stratospheric AOD after the 2011 eruption of Nabro volcano measured by lidars over the Northern Hemisphere, *Environ. Res.  
Lett.*, 7, 034013, doi:10.1088/1748-9326/7/3/034013, 2012.

- Sioris, C. E., Boone, C. D., Bernath, P. F., Zou, J., McElroy, C. T., and McLinden, C. A.: Atmospheric chemistry experiment (ACE) observations of aerosol in the upper troposphere and lower stratosphere from the Kasatochi volcanic eruption, *J. Geophys. Res.*, 115, d00L14, doi:10.1029/2009JD013469, 2010.
- Smith, W. J.: *Modern Optical Engineering*, McGraw-Hill, New York, 2000.
- 5 Solomon, S., Daniel, J. S., Neely, R. R., Vernier, J.-P., Dutton, E. G., and Thomason, L. W.: The persistently variable background stratospheric aerosol layer and global climate change, *Science*, 333, 866–870, doi:10.1126/science.1206027, 2011.
- Stocker, T. F., Qin, D., Plattner, G.-K., Tignor, M. M., Allen, S. K., Boschung, J., Nauels, A., Xia, Y., Bex, V., and Midgley, P. M.: *Climate Change 2013, The Physical Science Basis*, Cambridge University Press, Cambridge, UK and New York, USA, 2013.
- Suhre, D. R., Denes, L. J., and Gupta, N.: Telecentric confocal optics for aberration correction of acousto-optic tunable filters, *Appl. Optics*, 43, 1255–1260, doi:10.1364/AO.43.001255, 2004.
- 10 [Taha, G., Rault, D. F., Loughman, R. P., Bourassa, A. E., and von Savigny, C.: SCIAMACHY stratospheric aerosol extinction profile retrieval using the OMPS/LP algorithm, \*Atmos. Meas. Tech.\*, 4, 547–556, doi:10.5194/amt-4-547-2011, 2011.](#)
- Thomason, L. W. and Taha, G.: SAGE III aerosol extinction measurements: initial results, *Geophys. Res. Lett.*, 30, 1631, doi:10.1029/2003GL017317, 2003.
- 15 Thomason, L. W. and Vernier, J.-P.: Improved SAGE II cloud/aerosol categorization and observations of the Asian tropopause aerosol layer: 1989–2005, *Atmos. Chem. Phys.*, 13, 4605–4616, doi:10.5194/acp-13-4605-2013, 2013.
- Uchida, N.: Optical properties of single-crystal paratellurite ( $\text{TeO}_2$ ), *Phys Rev. B*, 4, 3736–3745, doi:10.1103/PhysRevB.4.3736, 1971.
- Vanhellemont, F., Tetard, C., Bourassa, A., Fromm, M., Dodion, J., Fussen, D., Brogniez, C., Degenstein, D., Gilbert, K. L., Turnbull, D. N., Bernath, P., Boone, C., and Walker, K. A.: Aerosol extinction profiles at 525 nm and 1020 nm derived from ACE imager data: comparisons with GOMOS, SAGE II, SAGE III, POAM III, and OSIRIS, *Atmos. Chem. Phys.*, 8, 2027–2037, doi:10.5194/acp-8-2027-2008, 2008.
- 20 Vernier, J.-P., Thomason, L., and Kar, J.: CALIPSO detection of an Asian tropopause aerosol layer, *Geophys. Res. Lett.*, 38, L07804, doi:10.1029/2010GL046614, 2011a.
- Vernier, J.-P., Thomason, L. W., Pommereau, J.-P., Bourassa, A., Pelon, J., Garnier, A., Hauchecorne, A., Blanot, L., Trepte, C., Degenstein, D., and Vargas, F.: Major influence of tropical volcanic eruptions on the stratospheric aerosol layer during the last decade, *Geophys. Res. Lett.*, 38, 112807, doi:10.1029/2011GL047563, 2011b.
- 25 Vernier, J.-P., Thomason, L. W., Fairlie, T. D., Minnis, P., Palikonda, R., and Bedka, K. M.: Comment on “Large volcanic aerosol load in the stratosphere linked to Asian monsoon transport”, *Science*, 339, 647, doi:10.1126/science.1227817, 2013.
- Voloshinov, V.: Spectral and polarization analysis of optical images by means of acoustooptics, *Optics Laser Technology*, 28, 119–127, doi:10.1016/0030-3992(95)00079-8, 1996.
- 30 Voloshinov, V. B. and Mosquera, J. C.: Wide-aperture acousto-optic interaction in birefringent crystals, *Opt. Spectrosc.*, 101, 635–641, doi:10.1134/S0030400X06100225, 2006.
- Voloshinov, V. B., Yushkov, K. B., and Linde, B. B. J.: Improvement in performance of a  $\text{TeO}_2$  acousto-optic imaging spectrometer, *J. Opt. A-Pure Appl. Op.*, 9, 341–347, doi:10.1088/1464-4258/9/4/006, 2007.
- von Savigny, C., Ernst, F., Rozanov, A., Hommel, R., Eichmann, K.-U., Rozanov, V., Burrows, J. P., and Thomason, L. W.: Improved stratospheric aerosol extinction profiles from SCIAMACHY: validation and sample results, *Atmos. Meas. Tech. Discuss.*, 8, 8353–8383, doi:10.5194/amtd-8-8353-2015, 2015.
- 35 Winker, D. M., Hunt, W. H., and McGill, M. J.: Initial performance assessment of CALIOP, *Geophys. Res. Lett.*, 34, L19803, doi:10.1029/2007GL030135, 2007.

**Table 1.** ALI final system optical parameters.

Parameter	Value
Effective focal length (mm)	74.3
Front end magnification	0.67
Back end magnification	1.27
Entrance Pupil (mm)	9.91
Field of view (°)	$6.0 \times 5.0$
F-number	7.5
Image size (mm)	$9 \times 7.5$
Image size (pixels)	$1000 \times 800$
Resolved image size (averaged pixels)	$143 \times 114$
Spectral range (nm)	650–950

Wiscombe, W. J.: Improved mie scattering algorithms, *Appl. Optics*, 19, 1505–1509, 1980.

Xu, J. and Stroud, R.: *Acousto-Optic Devices: Principles, Design, and Applications*, Vol. 12, Wiley-Interscience, New York, USA, 1992.

Zawada, D. J., Dueck, S. R., Rieger, L. A., Bourassa, A. E., Lloyd, N. D., and Degenstein, D. A.: High-resolution and Monte Carlo additions to the SASKTRAN radiative transfer model, *Atmos. Meas. Tech.*, 8, 2609–2623, doi:10.5194/amt-8-2609-2015, 2015.

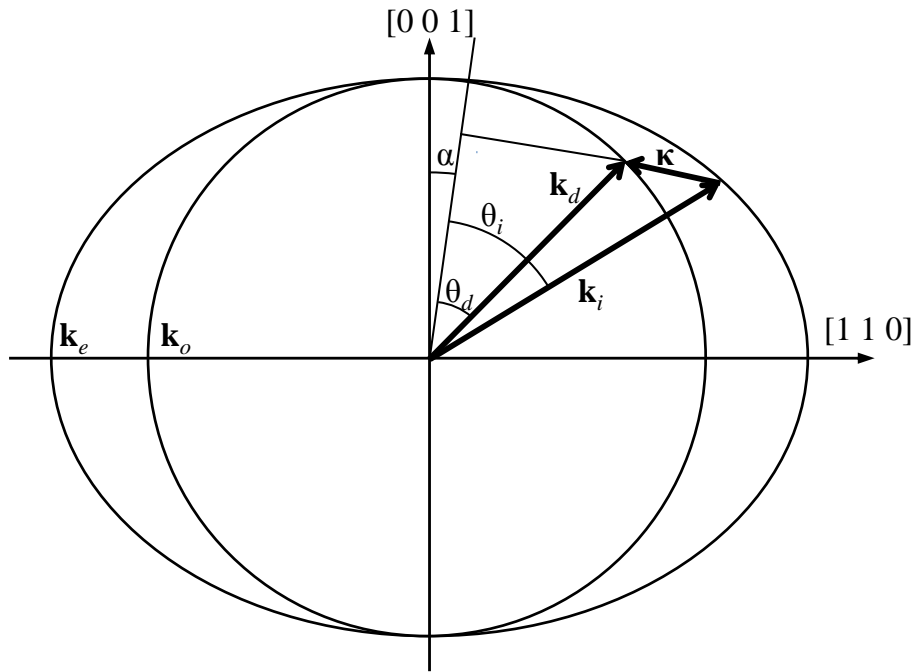


**Figure 1.** The wave vectors generated by the AOTF experiment. From Eq. (1), the incident wave vector,  $\mathbf{k}_i$ , diffracted wave vector,  $\mathbf{k}_d$ , and acoustic wave vector  $\boldsymbol{\kappa}$  are shown. The respective interaction angles for the incident and diffracted wave vectors  $\theta_i$  and  $\theta_d$  are also presented.



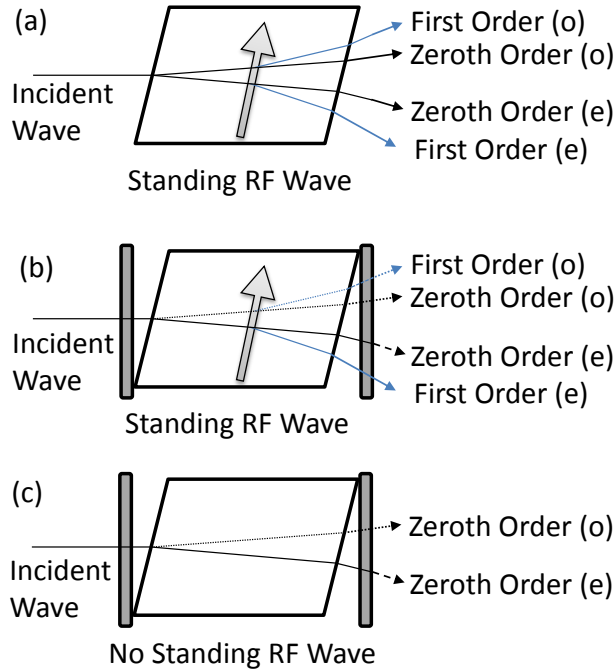


**Figure 2.** (a) An AOTF undergoing Bragg diffraction with an unpolarised incident wave with a RF wave applied represented by the arrow. After the diffraction event four output signals are formed: the zeroth order and first order ordinary (o) and extraordinary (e) signals. However the only optical path that remains at a constant angle no matter the applied RF wavelength is the first order extraordinary diffracted signal. (b) Two linear polarizers are added to the system, the first linear polarizer removes the ordinary polarization removing the outputs with the dotted lines and the second linear polarizer removes undiffracted extraordinary light shown by the dashed line. (c) The system in (b) without a RF wave so Bragg diffraction is occurring. Once again the first linear polarizer removes the ordinary polarization represented by the dotted line and the second linear polarizer removes the extraordinary light shown by the dashed line.

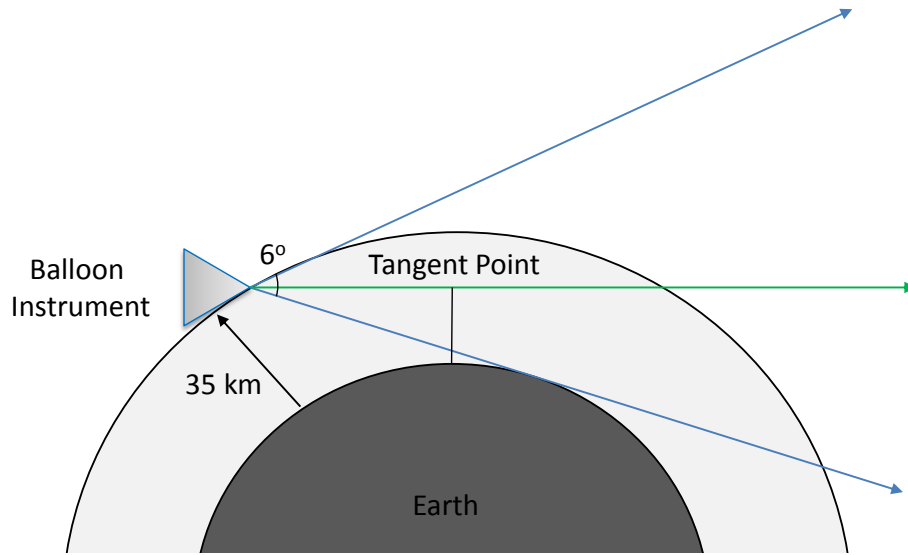


**Figure 3.** ALI in a stratospheric balloon geometry showing the complete  $6^\circ$  field of view in blue with a float altitude of 35 km. The green line shows a typical vertical line-of-sight where the tangent point or altitude is set by the minimum distance between the earth and the line-of-sight.

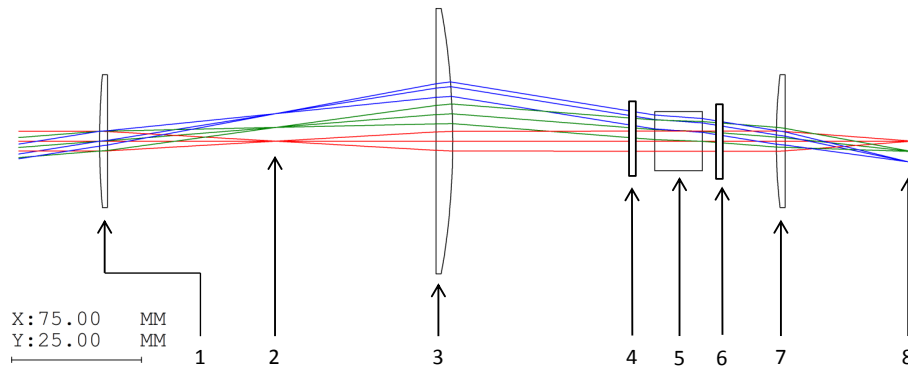


**Figure 4.** Ray Tracing diagram of the telescopic lens system for ALI simulated by Code V optical design software. The elements in the system are the following: (1) 150 mm focal length plano-convex lens. (2) Field stop. (3) 100 mm focal length plano-convex lens. (4) Vertical linear polarizer. (5) Brimrose AOTF. (6) Horizontal linear polarizer. (7) 50.4 mm focal length bi-convex lens. (8) Imaging plane.

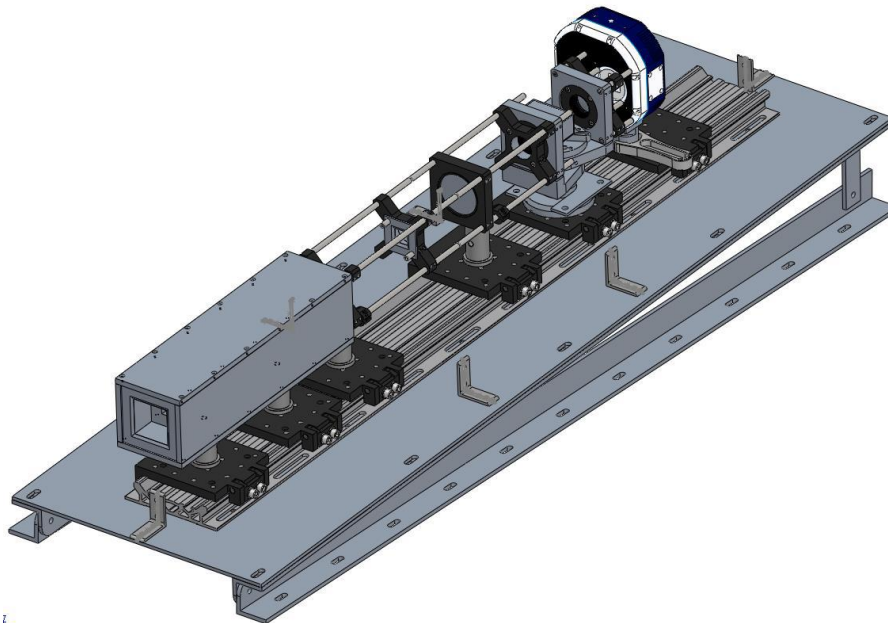


**Figure 5.** An isometric view of the complete ALI system with the baffle and 3° slant required to correctly position the field of view. Light tight case absent from diagram.

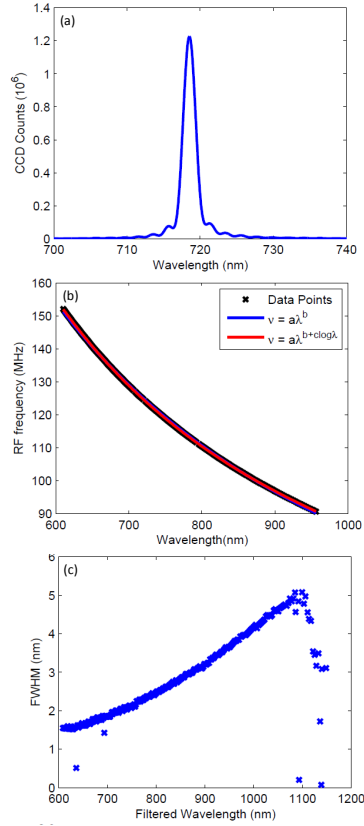


**Figure 6.** (a) A spectrum taken from the AOTF from the point spread function when the tuning frequency of the AOTF was at 124.96 MHz. (b) The calibration curves for the AOTF tuning curve which contains the data points recorded and fit curve. (c) The full width half max for each of the determined wavelengths for the AOTF. The full width half max at 600 nm is 1.5 nm and as the wavelengths get longer it increases to 4.9 nm at 1080 nm.

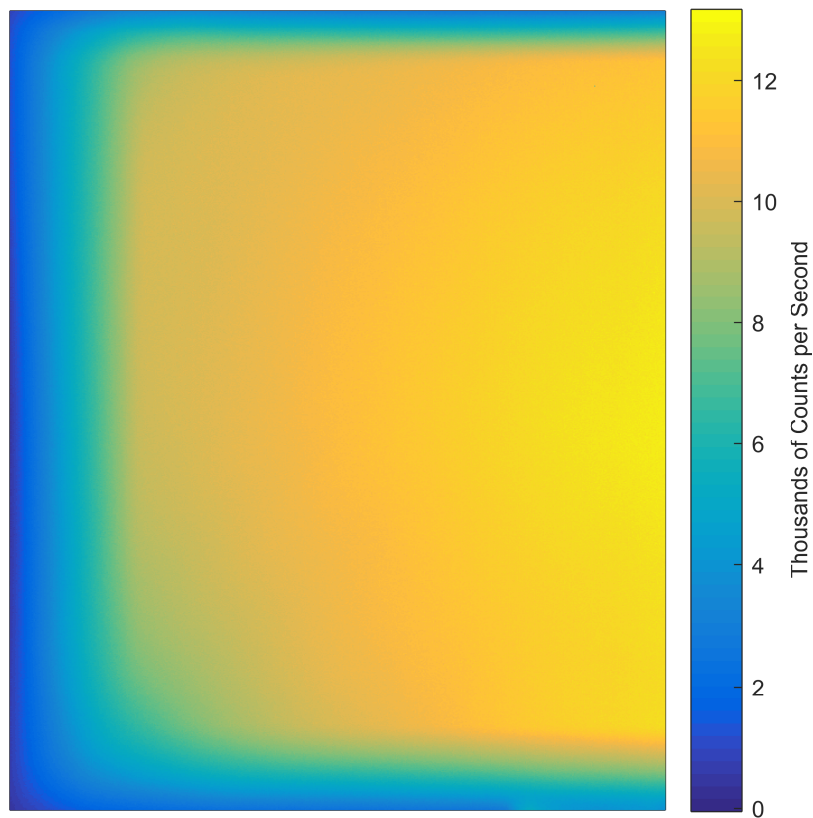


**Figure 7.** A calibration image after stray light removal has been performed where the measured wavelength is 750 nm with a 1 s exposure time. Vignetting can be seen as moving away from center of the image. Additionally the last  $1^\circ$  of the horizontal field of view ~~is~~ on the right side is lost due to strong contamination from reflections within the system.

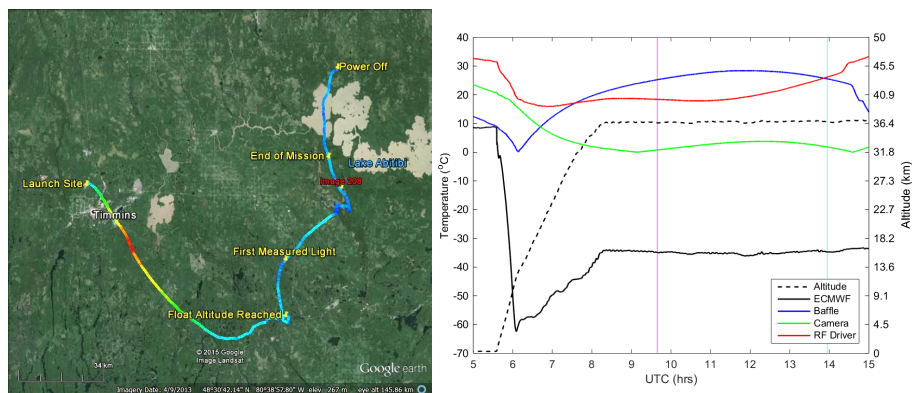


**Figure 8.** (a) The GPS data from ALI during the Nimbus 7 mission generated via Google Earth. The colour of the line represents the absolute speed of the gondola during the mission and the blue, green, red colours represent speeds of approximately 10, 70, and 140 km/h. Important landmarks are noted on the image. The end of mission represent the end of the aerosol mission. No GPS data was collected from ALI after power down. The location of image 208 is the red label. (b) The temperature and altitude profiles from the NIMBUS 7 flight. The time of image 208 is shown by the cyan vertical line and first light measured by ALI is occurs at-represented by the magenta vertical line.

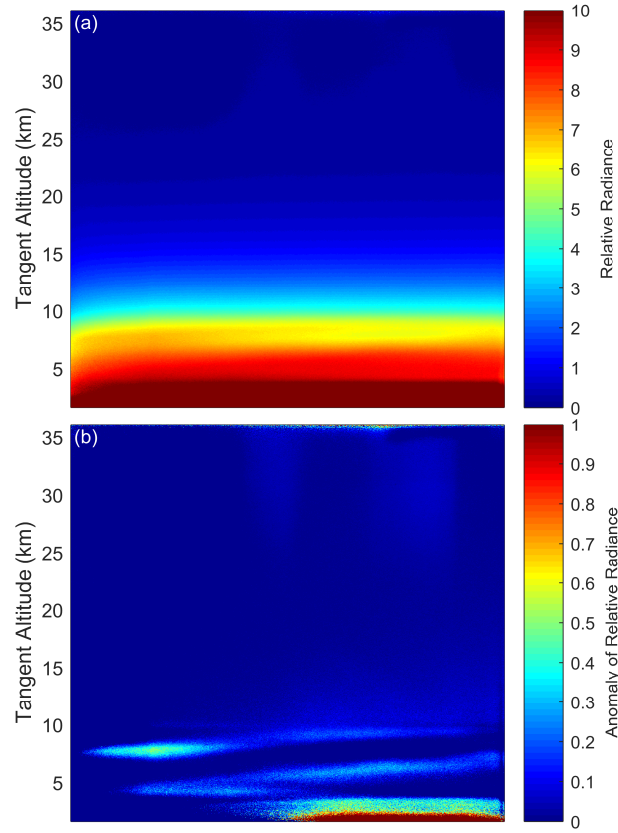


**Figure 9.** (a) Final calibrated 750 nm image, taken at 13:57 UTC located at  $48.55^{\circ}$  N,  $80.00^{\circ}$  W with a solar zenith angle and solar scattering angle of  $63^{\circ}$  and  $98^{\circ}$  respectively. (b) The same 750 nm image with the mean of the profile removed from the image leaving the residual signal that shows thin clouds in the troposphere.



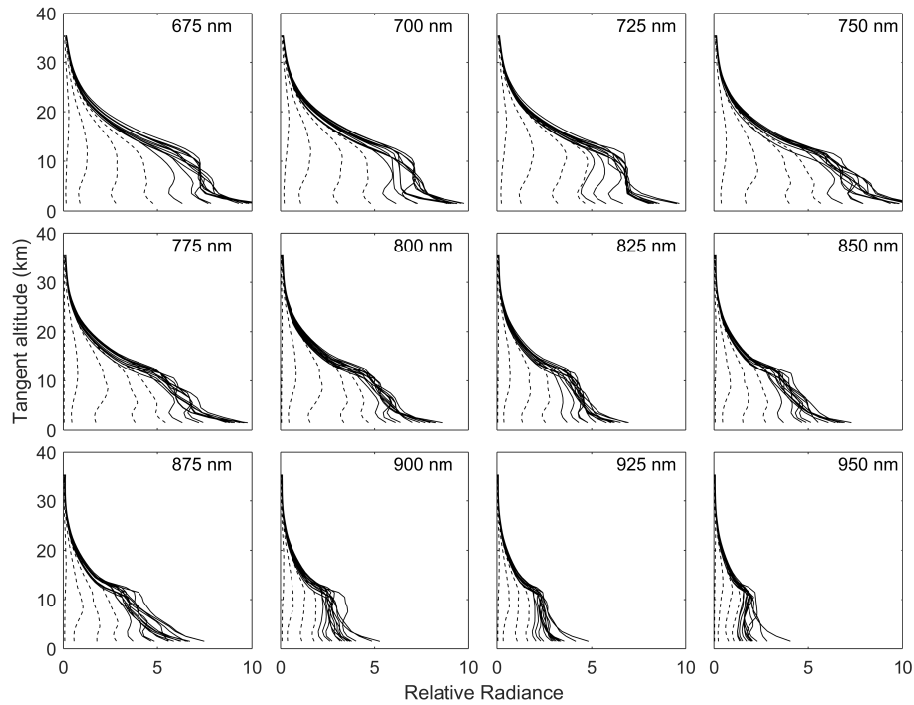


**Figure 10.** Averaged ALI relative radiance vectors from 12 of the 13 wavelengths from the NIMBUS-7 flight. Each panel presents the radiance vectors from a different wavelength measured which is denoted in the top right corner. The dashed lines are radiance profiles where the solar zenith angle is greater than  $90^\circ$  and solid lines are profile where the solar zenith angle is less than  $90^\circ$ . The separation between each consecutive radiance vector at each wavelength is approximately 2 degrees in solar zenith angle.

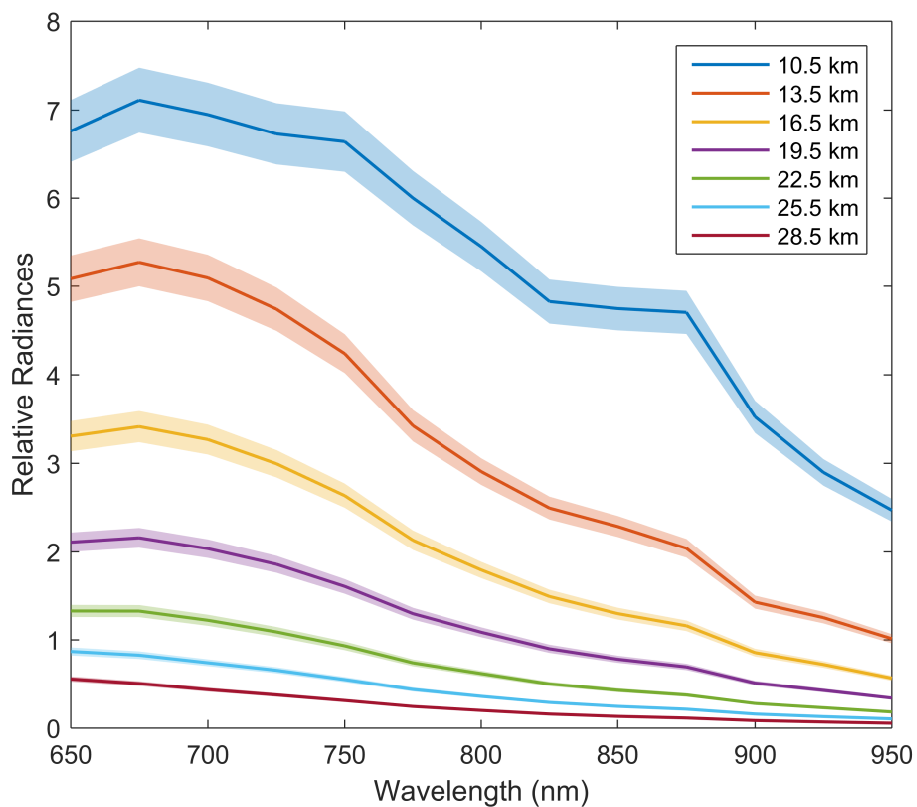


**Figure 11.** Level 1 relative radiances spectrally from 650 to 950 nm as measured from ALI at approximately 14:20 UTC consisting of images number 204 to 216 looking  $90^\circ$  in the azimuth from the sun facing southwards. These spectral profiles are presented at several tangent altitudes with a horizontal look direction of  $0^\circ$ . The shading represents the error on the radiances.

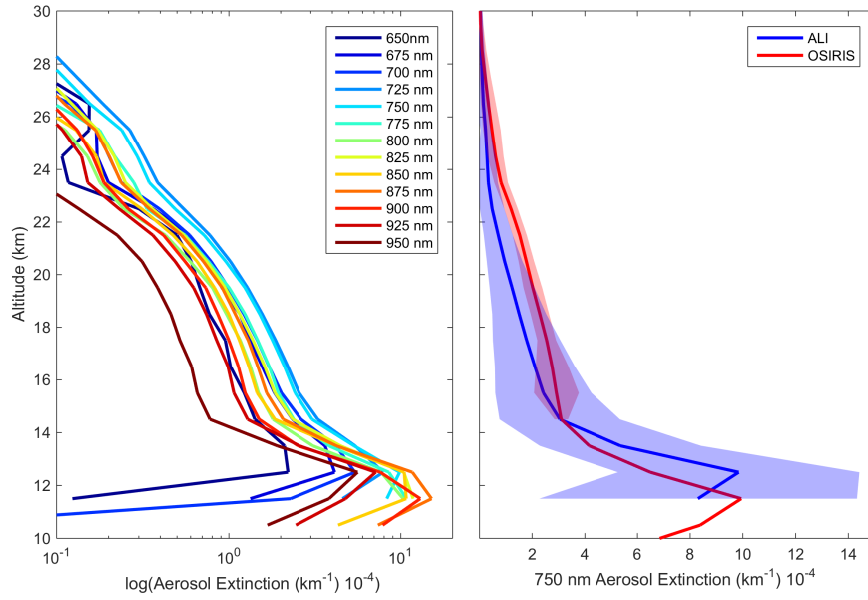


**Figure 12.** Left is the retrieved aerosol extinction profiles from the last complete imaging cycle consisting of images 205 to 216 from the 0.0° horizontal line-of-sight. Right is the 750 nm ALI aerosol extinction in blue ~~with its error represented by the shading~~ compared to the 750 nm extinction measured by OSIRIS in ~~green~~red with its error represented by the respective shading.

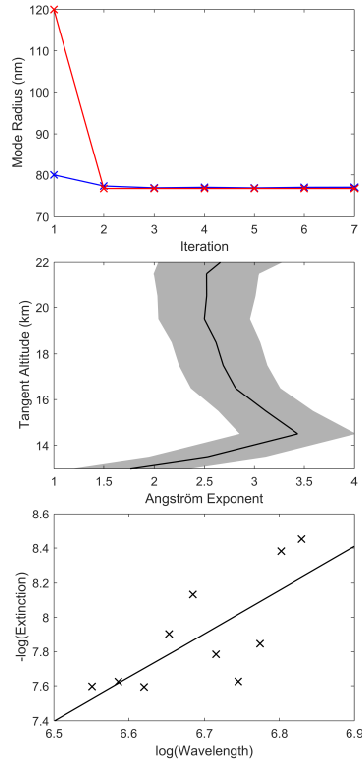


**Figure 13.** The top panel shows the convergence of two sample particle size retrievals, blue and red represent an initial state of 0.08 and 0.12  $\mu\text{m}$  mode radius respectively. Both initial states converge to the same value over approximately 3 iterations in the particle size retrieval method. The middle panel shows the final Angström exponents determined from images 204–216. The shading represents the error associated with the least squares fit. The bottom panel shows a typical least squares fit of the retrieved extinction values over wavelength to determine the Angström exponent at model altitude of 14.5 km.